2023-09

Experimental and numerical investigation on thermal properties of alkali-activated concrete at elevated temperatures

Yu, M

https://pearl.plymouth.ac.uk/handle/10026.1/21603

Experimental and numerical investigation on thermal properties of alkali-activated concrete at elevated temperatures

Min Yu [a,b], Hanjie Lin [b], Tan Wang [b], Feiyu Shi [a], Dawang Li [a,c], Yin Chi [b], Long-yuan Li [a,*]

[a] *School of Engineering, Computing and Mathematics, University of Plymouth, Plymouth, PL4 8AA, UK*
[b] *School of Civil Engineering, Wuhan University, Wuhan, 430072, China*
[c] *Guangdong Provincial Key Laboratory of Durability for Marine Civil Engineering, Shenzhen University, Shenzhen, 518060, China*

ARTICLE INFO

ABSTRACT

This paper presents the experimental and numerical investigation on the thermal properties of steel fibre-reinforced alkali-activated concrete (AAC) made by using multiple precursors at elevated temperatures. The temperature-dependent thermal properties such as mass change, thermal conductivity, density, specific heat, and thermal expansion are reported. The effects of temperature heating AAC, coarse aggregate, and steel fibre on the thermal performance of AAC are evaluated quantitatively. Experimental results show that high temperature greatly affects the thermal properties of AAC. Coarse aggregate and steel fibre also have a considerable influence on the thermal properties. Based on the test results, a multi-phase mesoscale model is developed to predict the thermal properties considering volume fractions of steel fibre and coarse aggregate, which can be used in the fire safety design of AAC structures.

1. Introduction

Concrete, as one of the main construction materials, has been widely used in construction and building industries. Traditionally, concrete is produced by means of mixing aggregate and water with Portland cement via the process of hydration reaction. However, the production of Portland cement produces a large amount of CO_2 emissions, which is harmful and not sustainable to earth. It is estimated that the production of every 1 kg of cement produces about 0.87 kg CO_2 emissions [1]. For this reason, searching for alternative binders is particularly important and is the area where many researchers are of interest. Geopolymer, as a type of alkali-activated binder, is a cementitious material formed by aluminosilicate material via the process of geo-polymerization. It is estimated that by using geopolymer to replace traditional Portland cement in concrete, the CO_2 emissions can be reduced by approximately 80% [2]. In addition, concrete made from geopolymer has the advantages of fast hardening, strong early strength, dense aggregate-matrix interface, solidifying toxic metal ions, high heat resistance, and high freeze-thaw cycle resistance.

Metakaolin (MK) [3], fly ash (FA) [4] and ground granulated blast furnace slag (GGBS) [5] are the main sources of aluminosilicate-rich materials for producing alkali-activated binder. GGBS is a self-cementing material which is a by-product of the steel production industry. It was reported that about 170–250 million tons of GGBS are produced per year in the world [6]. In addition, GGBS has positive effects on the setting, workability, and early strength of the alkali-activated concrete (AAC) cured in ambient conditions. Thus, AAC with GGBS have greater applications in practical engineering.

---

* Corresponding author.
E-mail address: long-yuan.li@plymouth.ac.uk (L.-y. Li).

Although alkali-activated binder (AAB) has many advantages, its drying shrinkage is an issue that the design engineers have some concerns since the shrinkage of AAB can seriously affect the performance of AAC structures. A study carried out by Eisa et al. [7] showed that the geogrid reinforcement in MK-based geopolymer concrete could greatly reduce the drying shrinkage strain. The addition of steel fibre in concrete can disperse the shrinkage stress of the capillary in the matrix, effectively alleviating the local stress concentration. At the same time, there is a large friction between the steel fibre and the concrete matrix, which can effectively prevent the expansion of micro-cracks in the concrete, thus reducing the shrinkage of the concrete [8,9]. Moreover, the addition of steel fibre in concrete can strengthen and toughen the concrete, resulting in better mechanical properties of bending resistance, compressive and tensile strengths, shear resistance, abrasion resistance, and impact toughness [10–12]. When the volume fraction of coarse aggregate in concrete increases, the amount of AAB used in concrete decreases respectively, and the corresponding cost can be effectively reduced while the shrinkage of concrete can also be limited. Besides, overall stability and strength of concrete can be improved due to the interlocking actions between the aggregate particles [13]. Therefore, the use of steel fibre and coarse aggregate in AAC should be encouraged.

Fire is one of the most common natural or human-induced disasters in building structures, and thus structural fire protection has become an important part of the design of the whole life cycle of engineering structures. The fire resistance of a structure at elevated temperatures is dependent on the instantaneous temperature field as well as the thermal-induced stresses. Thermal properties such as thermal conductivity, density, specific heat, and thermal expansion are the basic physical parameters required for the calculation of the temperature and thermal-induced stresses. In literature numerous studies have been carried out for evaluating the thermal properties of concrete. For example, the thermal conductivities of normal strength concrete [14], high strength concrete [15], self-consolidating concrete [16], and reactive power concrete [17] at various elevated temperatures were investigated and the influences of temperature, fibre, and coarse aggregate on the thermal conductivity were discussed. In the experimental investigations, the specific heat can be measured by using differential scanning calorimeter (DSC) and differential thermal analyser (DTA) for small samples of 1 mg–10 mg [18,19], or by using the inverse technique for large samples [20]. The linear thermal expansion may be measured by using dilatometry or thermo-mechanical analysis. For instance, Johnson and Parsons [21], Ghannam [22], Siddiqui and Flower [23] studied the thermal expansion of concrete and the influencing factors such as mix design, type of cement, specimen size, temperature, and the age of the specimen. Some empirical formulas are provided in Europa [24] and America [25] for the thermal conductivity, specific heat, density, and thermal expansion of normal strength concrete at elevated temperatures.

The above-mentioned studies evoke a fundamental understanding of the thermal properties and performance of concrete materials at ambient and elevated temperatures. Apparently, with the increasing usage of AAC in a broad range of construction industries, the thermal properties and performance of AAC are attracting more and more attention to both the academic researchers and practical engineers. However, to the authors' best knowledge, research work on the testing and/or predicting effective thermal properties of AAC are still very limited, especially at elevated temperatures. In this paper, we present the experimental and numerical investigations on the thermal properties of AAC with and without steel fibre at various elevated temperatures. The experimental work involves the measurement of mass loss, thermal conductivity, specific heat, and thermal expansion of AAC with different mix designs at various
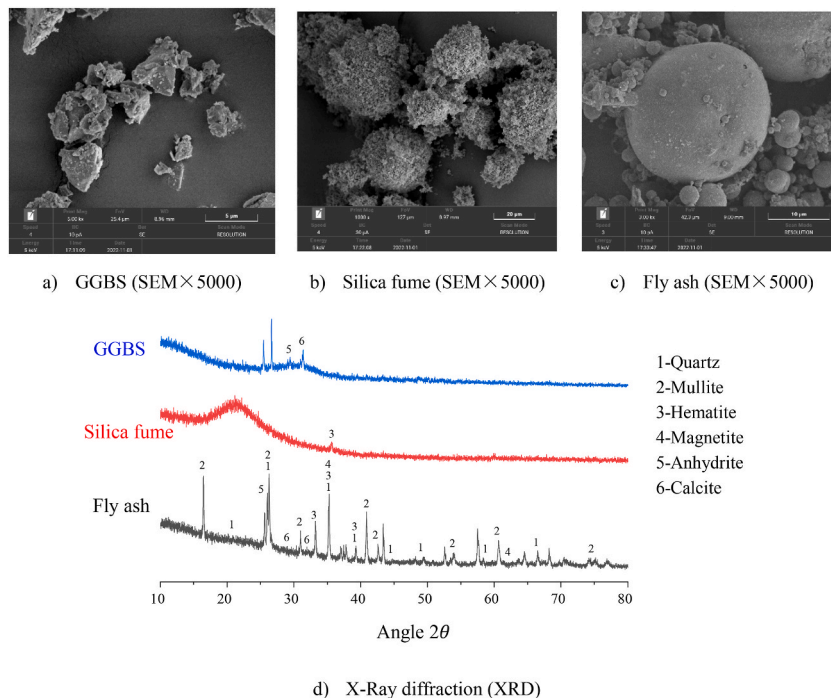

a) GGBS (SEM×5000) b) Silica fume (SEM×5000) c) Fly ash (SEM×5000)

1-Quartz
2-Mullite
3-Hematite
4-Magnetite
5-Anhydrite
6-Calcite

Angle 2θ

d) X-Ray diffraction (XRD)

Fig. 1. Microstructures of precursor materials.

elevated temperatures. In the numerical work we developed a three-phase model for simulating the heat transfer in the steel fibre-reinforced AAC. By using the temperature results obtained from the three-phase model, the effective thermal conductivity and effective specific heat of the steel fibre-reinforced AAC are also calculated.

2. Materials and experiments

2.1. Materials and mix design

The raw materials used to make AAC samples are the precursors, alkali activator, admixture, and aggregate. GGBS, FA, and silica fume (SF) were used as the combined precursors. Both the GGBS and FA are the industrial waste materials. GGBS can dissolve to form gel in the alkaline solution. FA can retard the setting time of fresh concrete. SF is frequently used as a binding material since it contains silicon dioxide, calcium oxide and aluminium oxide. The combined use of these three precursors as the binder material in AAC can improve the properties of both the fresh and hardened concretes [5]. Fig. 1 shows the microstructure images of GGBS, FA and SF obtained from our SEM tests and the main chemical components in them obtained from our XRD tests. The physical properties of GGBS, FA and SF are provided in Table 1. Flake industrial caustic soda (95% NaOH) with density of 2.13 g/cm^3 and sodium silicate (30% SiO_2, Na_2O) with density of 1.51 g/cm^3 and pH of 10–13 were used as the alkali activator. The straight steel fibre was used as an admixture. The steel fibre has the length of 12 mm and aspect ratio of 45. The nominal tensile strength of the steel fibre is about 2750 MPa. The fine aggregate used in the mix was the river sand specified in standard GB/T 14684–2011 with a fineness modulus of 2.7. The coarse aggregate used in the mix was the crushed stone with the sizes ranging from 5 mm to 25 mm, and their grading complies with the requirements of ASTM C33. The sand-to-binder ratio used in the mix was set as 0.9 for all tested samples. The volume fraction of the steel fibre in the mix was 0% or 2%. The volume fraction of the coarse aggregate in the mix was set to 0% or 30%. For the classification of the samples tested, the mix designs are labelled as 'SiiCAjj', in which 'S' denotes the steel fibre and 'ii' refers to the volume fraction, 'CA' represents the coarse aggregate and 'jj' is the corresponding volume fraction. The mixing design employed in the present study is shown in Table 1, which was based on the results obtained from our previous works on AAC [5] and on steel fibre-reinforced concrete [10].

2.2. Preparation of samples

The following steps were used for the preparation of samples (see Fig. 2).

1) Prepare the moulds for cylinders (50mm × 100 mm), prisms (114mm × 64mm × 230 mm), and cubes (100mm × 100mm × 100 mm). A thermocouple was placed in the middle of the cubic mould.
2) GGBS, FA, SF, and aggregate were first mixed for 3 min.
3) Steel fibre was then added in and mixed with them for another 2 min.
4) Sodium hydroxide was dissolved in water for 5 min and then mixed with sodium silicate and stir the solution for 5 min.
5) The liquid mixture was then added into the solid mixture, and they were mixed for about 4 min.
6) The fresh AAC were poured into the mould and vibrated on the shaking table for about 1 min.
7) Samples were cured in the mould for 24 h in air in room temperature. After demould they were wet-cured for 28 days in room temperature, followed by a nature dry of another 28 days in laboratory room (~22 °C).
8) Polish the surfaces of concrete samples.

2.3. Experiments

Thermal properties, including the mass loss, thermal conductivity, specific heat, and linear thermal expansion of AAC samples, were measured by direct weighting, using the transient parallel hot wire method, the inverse approach, and the PCY high temperature vertical dilatometers, respectively. Fig. 3 summarizes the sample sizes, thermal equipment and test set-up, and heating modes employed in the tests. The compressive strengths of the mixtures at the ambient temperature were also determined experimentally and the corresponding results are shown in Table 1 for the reference.

(1) **Mass loss:** After a sample was exposed to an elevated temperature, the change of the internal compositions of the sample led to some loss of mass, which is a measure for evaluating the temperature resistance of the material. The cubic samples shown in

Table 1
Mix design of alkali-activated concrete (units: kg/m^3).

Mix No.	Mix design of alkaline activated mortar/concrete									Cylinder strength (MPa)
	GGBS	FA	SF	Fine aggregate	Water	Sodium silicate	NaOH	Steel fibre	Coarse aggregate	
S0CA0	703 (0.7)	201 (0.2)	100 (0.1)	1105 (1.1)	229 (0.23)	254 (0.25)	6.77 (0.007)	\	\	50.78
S2CA0	689 (0.7)	197 (0.2)	98 (0.1)	1083 (1.1)	224 (0.23)	249 (0.25)	6.63 (0.007)	157 (2%)	\	81.72
S0CA30	492 (0.7)	141 (0.2)	70 (0.1)	774 (1.1)	160 (0.23)	178 (0.25)	4.74 (0.007)	\	900 (30%)	66.69
S2CA30	483 (0.7)	138 (0.2)	69 (0.1)	758 (1.1)	157 (0.23)	174 (0.25)	4.64 (0.007)	109.9 (2%)	900 (30%)	75.70

a) Manufacturing mold - cylinder   b) Manufacturing mold - cuboid   c) Arrange thermocouple

d) Pouring   e) Curing   f) Grooving
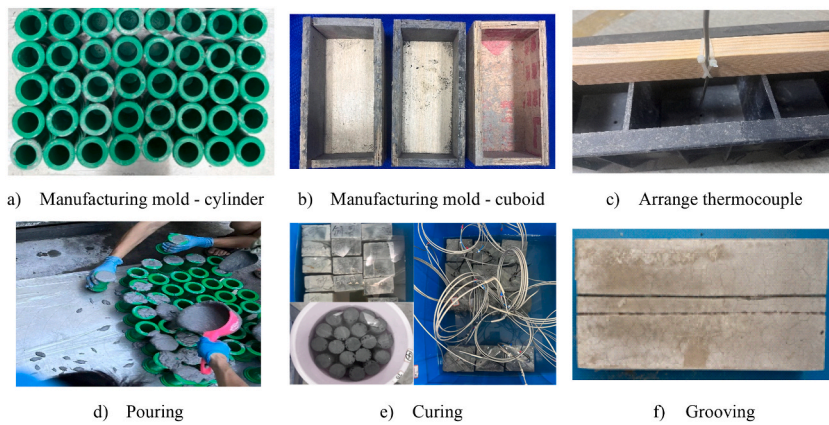
Fig. 2. Schematic of the preparation of AAC samples.

Fig. 3. Schematic summation of thermal tests.

Fig. 3 were used for the tests of mass loss. The mass of the sample was first recorded at room temperature before the test and then it was heated to a target temperature (e.g., 20 °C, 100 °C, 300 °C, 500 °C, 700 °C, 900 °C). After the target temperature was reached the sample was kept in that temperature for about 1 h. After then, the sample was cooled down to the room temperature and then its mass was recorded again. The mass loss was calculated based on the initially measured mass at the ambient temperature before the heating and the finally measured mass after the heating and cooling. For each target temperature, three samples were repeatedly tested for each mix type. The average value from the three repeat tests was taken and reported.

(2) **Thermal conductivity:** Thermal conductivity is defined as the heat passing through the unit isothermal area of a material in unit time under unit temperature gradient. Transient parallel hot wire method, one of the commonly used methods for measuring the thermal conductivity, was employed in our tests. According to the Chinese Design Codes [26], the prism samples shown in Fig. 3 were used in the tests. The thermal conductivity was measured at the temperatures 20 °C (as room temperature),

100 °C, 200 °C, 300 °C, 400 °C, 500 °C, 600 °C, 700 °C, 800 °C, and 900 °C, respectively, during the heating process of the sample. After it was heated to 900 °C, the sample was cooled down gradually to the room temperature. During the cooling process the thermal conductivity of the sample was measured again at the temperatures 800 °C, 700 °C, 600 °C, 500 °C, 400 °C, 300 °C, 200 °C, 100 °C, and 20 °C, respectively. For each mix type three samples were repeatedly tested. The average value from the three repeat tests was taken and reported.

(3) **Specific heat:** Specific heat is defined as the heat absorbed when the temperature rises by 1 °C for a material with unit mass. Specific heat is usually obtained by using an inverse approach. Previous research has found that the solution of the heat equation satisfies the conditions of existence, uniqueness, and stability, so the specific heat solution of the inverse process must also be unique and stable. To find the specific heat of a material using inverse solution, the time-dependent temperature curve of the central point of a sample is produced first based on the collected experimental data of the thermocouple. A three-dimensional finite element analysis model was developed to simulate the heat transfer of the sample used in laboratory tests to obtain a temperature history curve that is most close to that of the test data by searching for the optimal value of specific heat using the gradient method. In the present study, cubic samples shown in Fig. 3 were used to record the temperature history during the heating process of the sample. Again, for each mix type three samples were repeatedly tested. The average value from the three repeat tests was taken and reported.

(4) **Thermal expansion:** Thermal expansion coefficient is an important parameter, which has great influence on the thermal stress generated in a material when the temperature is not uniformly distributed in the material. In the present study the PCY high temperature vertical dilatometer was used to measure the axial thermal expansion of the cylindrical samples as shown in Fig. 3. During the test the sample was successively heated to the target temperatures, from 20 °C to 100 °C, 200 °C, 300 °C, 400 °C, 500 °C, 600 °C, 700 °C, 800 °C, and 900 °C. After a target temperature was reached the sample was kept in that temperature for about 1 h to obtain a relative uniform temperature field and then the measurement was taken for the thermal expansion at that temperature. Again, for each mix type three samples were repeatedly tested. The average value from the three repeat tests was taken and reported.

3. Experimental results and discussion

3.1. Experimental observations

Fig. 4 shows the morphology of AAM and AAC samples with and without steel fibre, after they were exposed to various elevated temperatures. It can be seen from the figure that, with the increase of exposure temperature the steel fibre and coarse aggregate remained stable and integration. However, their colour turned much dark due to the reaction of oxidation. The alkali-activated matrix got darker and looser, and the pores in the matrix become large and more visible after they were exposed to elevated temperatures. Note that AAM or AAC are often subjected to shrinkage and/or cracking, particularly when they are exposed to high temperature. Microcracks were found in the samples after they had a heating process. However, no large cracks or spalling were found in the tested samples. This means that the experimentally obtained thermal properties presented in the present study may have included the effect of microcracks and micro-structure changes.

3.2. Residual density

Fig. 5 plots the changes of density and relative density of AAM and AAC samples with and without steel fibre after they were exposed to elevated temperatures. It can be seen from the figure that the mass loss was quicker in the two AAM samples than in the two AAC samples, which is expected as the mass loss in the sample is mainly contributed by the geopolymer products rather than by the
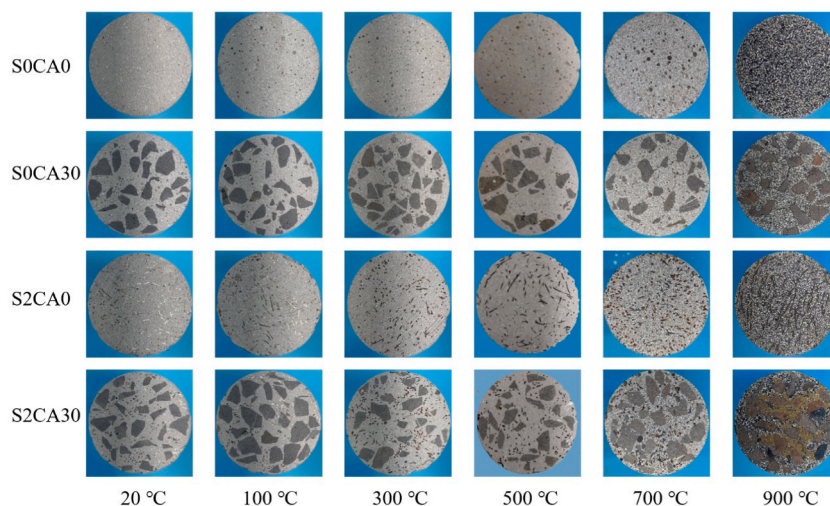

Fig. 4. Morphology of AAM and AAC samples after exposed to elevated temperatures.
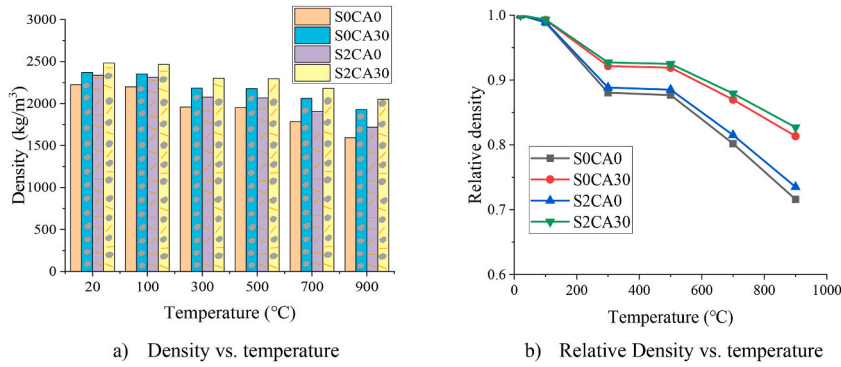
Fig. 5. Density change of AAM and AAC samples after exposed to elevated temperatures.

aggregate or steel fibre. The mass loss in the AAM or AAC sample with steel fibre is slightly slower than that in the AAM or AAC without steel fibre. Overall, for all tested samples the quick mass loss was found in the two temperature ranges; one is between 100 °C and 300 °C; and the other is between 500 °C and 700 °C. The former is due to the vaporisation of free water; whereas the latter is likely due to the release and followed by the evaporation of the chemically bound water in the matrix.

3.3. Thermal conductivity

Fig. 6 shows the variation of thermal conductivity of the AAM and AAC samples with and without steel fibre with exposure temperature when they were exposed to elevated temperatures. It can be seen from the figure that, for all tested samples the thermal conductivity obtained during heating process decreases with the increase of temperature. The decrease is much quicker in the AAC samples than in the AAM samples, and is slightly quicker in the steel fibre-reinforced AAC or AAM sample than in the non-reinforced AAC or AAM sample. In all tested samples, the AAM sample with steel fibre has the highest thermal conductivity; whereas the non-reinforced AAM sample or non-reinforced AAC sample has the lowest thermal conductivity when the temperature is below or over 200 °C. It is interesting to notice from the figure that, the thermal conductivity of individual samples does not vary very much with the temperature during its cooling process. This indicates that the material change mainly takes place during the heating process rather than in the cooling process. The difference between the thermal conductivity initially measured at the ambient temperature and that finally measured after the heating and cooling reflects the permanent effect of the temperature on the thermal properties of the material. The largest difference was found in the AAC sample with steel fibre, followed by the AAC sample without steel fibre, AAM sample with steel fibre, and AAM sample without steel fibre after they were exposed to the temperature 900 °C.

3.4. Specific heat

The temperature-history curves obtained from the central point of tested samples are plotted in Fig. 7. It is observed from the figure that the temperature-history curves of the samples with different mixes are very similar and are all below the furnace temperature curve because of the time required for the heat transfer. Unlike the furnace temperature that is linearly increased with time, the temperatures at the centre of the samples exhibit a repeated slow-fast increasing feature. The slow temperature increase in the sample is because some of the heat was used for the vaporisation of free water when the sample temperature is below 200 °C, and for the dehydration of C–S–H and/or C-A-S-H gels when the sample temperature is around 700 °C. The temperature jump inside the sample when the sample temperature is over 750 °C is likely due to the large thermal cracks which provide a short cut for the heat transfer in the sample.

The specific heat of the sample can be calculated by using the inversed method, based on the experimentally obtained temperature-
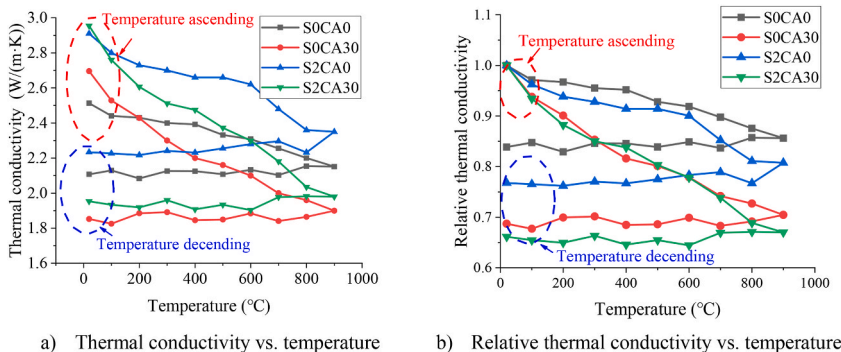

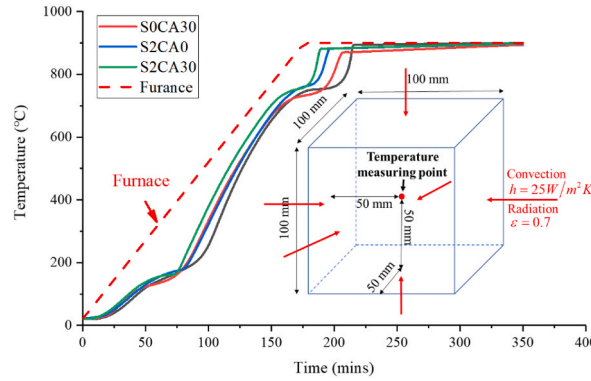Fig. 6. Thermal conductivity of samples at different temperatures.

Fig. 7. Temperature-history curves at the centre of the tested samples.

history curve as shown in Fig. 7 and the standard three-dimensional finite element analysis model to simulate the heat transfer of the sample used in the test. In the finite element analysis the geometry analysed was exactly the same as the sample size used in the test. All surfaces were assumed to expose to the environmental temperature recorded in the test. A uniform mesh of cubic elements ($20 \times 20 \times 20$) was used. The density and thermal conductivity used in the analysis were taken from the data obtained in Sections 3.2 and 3.3, respectively; whereas the specific heat was adjusted to best match the test results. Fig. 8 shows the results of the specific heat of the four samples obtained from the inverse method. It can be seen from the figure that the specific heat curves exhibit the up-down-flatten-up-down feature. The two "going up" parts correspond to the slow temperature increase in the temperature-history curve of the sample, whereas the two "going down" parts correspond to the fast temperature increase in the temperature-history curve of the sample, respectively. It is found from the calculated specific heat results that, the two AAM samples or the two AAC samples have nearly identical specific heat curves, indicating that the effect of steel fibre on the specific heat is negligible. Also, overall, the AAM samples have higher specific heat than the AAC samples regardless of the temperature, indicating that the specific heat of the coarse aggregate is smaller than that of the AAM.

3.5. Thermal expansion

Linear thermal expansion [27], $\gamma_l = (L_t - L_0)/L_0$, and corresponding thermal expansion coefficient, $\alpha_l = \gamma_l/(T_t - T_0)$, are calculated from the recorded lengths of the sample at various elevated temperatures, where L_o and L_t are the sample lengths at ambient temperature T_o and at elevated temperature T_t, respectively. Their results are plotted in Fig. 9. It can be seen from the figure that, for all tested samples the linear thermal expansion increases with the increased temperature until the temperature reaches to 500 °C, After then it decreases with the further increased temperature. After the temperature exceeds 800 °C, it has some recovery. The two AAM samples or the two AAC samples have almost the same linear thermal expansion regardless of the temperature, indicating that the effect of steel fibre on the thermal expansion is negligible. Also, overall, AAC samples have higher linear thermal expansion than the AAM samples, indicating that the thermal expansion in the coarse aggregate is higher than that in the mortar matrix in AAC samples. Previous studies reported that the high temperatures (>500 °C) could cause the recrystallization of geopolymer into secondary mineral phases and thus lead to the shrinkage of the volume of the geopolymer matrix [28,29]. Thus, whether the thermal expansion increases or decreases or whether it is positive or negative depends on which expansion in the geopolymer matrix or in aggregate is dominant.
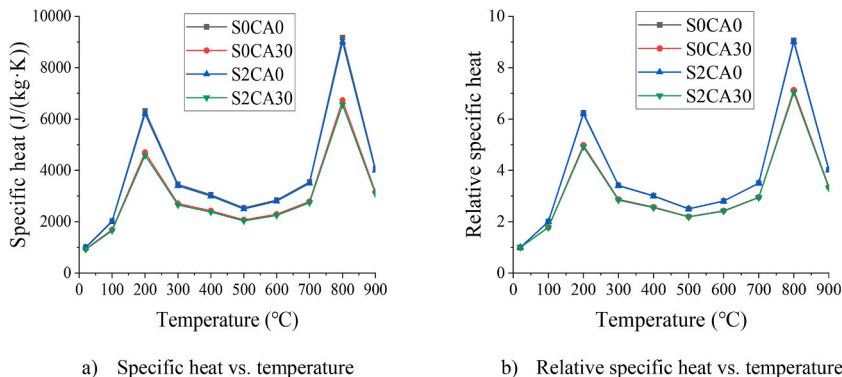

a) Specific heat vs. temperature

b) Relative specific heat vs. temperature

Fig. 8. Specific heat of concrete samples.

a)   Thermal expansion vs. temperature   b)   Expansion coefficient vs. temperature
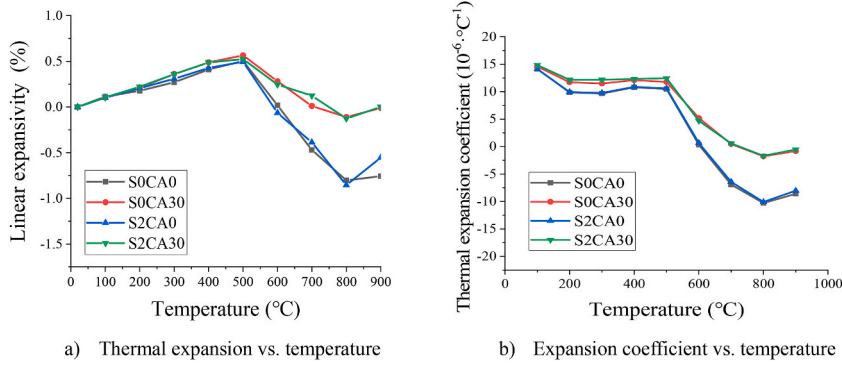
Fig. 9. Relationship between coefficient of thermal expansion and temperatures.

4. Mesoscale modelling of alkaline activated concrete at elevated temperatures

The experimental work on the thermal properties of concrete materials at elevated temperatures is not only expensive but also time-consuming because there are so many influencing parameters involved in the experimental tests. In order to understand the influence of different parameters on the thermal properties of concrete, a mesoscale model is developed herein to examine the individual effects of steel fibre and coarse aggregate on the thermal properties of the tested AAC samples.

4.1. Thermal analysis model of steel fibre reinforced alkaline activated concrete

In the present study the steel fibre-reinforced AAC is treated as a three-phase composite material, which contains a continuous AAM matrix phase embedded with the discrete, randomly distributed steel fibre phase and coarse aggregate phase. The latter are defined by their volume fractions in the mix. For AAC without steel fibre, zero volume fraction for steel fibre is assumed. For the simplicity of analysis, a two-dimensional, axisymmetric geometric model is employed to represent the cylindrical specimen, in which the width and highness of the two-dimensional, rectangular geometry represent the radius and length of the cylindrical specimen, respectively.

In the heat transfer analysis, the thermal conductivity, density, and specific heat of the AAM (matrix phase) are obtained by the regression analysis of the data from our tests as shown in the above section. The thermal conductivity and specific heat of the steel fibre are taken from European 4 [24] and Lie [30], respectively. The density of the steel fibre is assumed to be as a temperature-independent constant. The thermal conductivity and specific heat of the coarse aggregate are taken from Haenel et al. [31], Vosteen and Schellschmidt [32], respectively. The density of the coarse aggregate is also assumed to be as a temperature-independent constant. Tables 2–4 show the details of these parameters used in the present analysis.

Two sets of heat transfer analysis are carried out for determining the effective thermal conductivity and effective specific heat of the steel fibre-reinforced AAC. One is the steady state analysis for determining the effective thermal conductivity, in which the temperatures $T_{upper} = T + 2.5$ °C at upper boundary line and $T_{lower} = T - 2.5$ °C at lower boundary line are assumed where T is the target temperature taken from 20 °C to 900 °C, respectively, and the thermal insulation boundary condition is applied to both the left and right lines of the rectangular geometry. For each target temperature T, heat transfer finite element analysis is conducted. The heat flux obtained on the lower or upper boundary line is then used to calculate the effective thermal conductivity of the steel fibre reinforced AAC, as shown below,

Table 2
Thermal properties of Mortar.

Properties	Formula	Source
Thermal conductivity $W/(m \bullet k)$	$k_m = 2.48 - 0.2\left(\dfrac{T-20}{1000}\right) - 0.2\left(\dfrac{T-20}{1000}\right)^2$	Measured in our own tests presented in this study
Specific heat $J/(kg \bullet K)$	$C_{p,m} = \begin{cases} 468 + 5849 \cdot e^{\left(\frac{T-200}{76}\right)} & T \le 200°C \\ 2682 + 3635 \cdot e^{\left(\frac{200-T}{65}\right)} + 6457 \cdot e^{\left(\frac{T-800}{50}\right)} & 200 < T < 800°C \\ 2682 + 6457 \cdot e^{\left(\frac{800-T}{64}\right)} & T \ge 800°C \end{cases}$	
Density kg/m^3	$\rho_m = 2225 \begin{cases} 1 - 0.159\left(\dfrac{T-20}{1000}\right) - \left(\dfrac{T-20}{1000}\right)^2 & T \le 300°C \\ 0.877 & 300°C < T < 500°C \\ 0.877 - 0.39\left(\dfrac{T-20}{1000}\right) & T \ge 900°C \end{cases}$	

Table 3
Thermal properties of steel fibre.

Properties	Formula	Source
Thermal conductivity $W/(m \bullet k)$	$k_s = \begin{cases} 54 - 0.0333T & 20°C \leq T \leq 800°C \\ 27.3 & 800°C \leq T \leq 1200°C \end{cases}$	Eurocode 4 [24]
Specific heat $J/(kg \bullet K)$	$c_{p,s} = \begin{cases} 425 + 0.773T - 1.69 \cdot 10^{-3}T^2 + 2.22 \cdot 10^{-6}T^3 & 0°C \leq T \leq 600°C \\ 666 - \dfrac{13002}{T - 738} & 600°C < T \leq 735°C \\ 545 + \dfrac{17820}{T - 731} & 735°C < T \leq 900°C \\ 650 & T > 900°C \end{cases}$	
Density kg/m^3	$\rho_s = 7850$	

Table 4
Thermal properties of coarse aggregate.

Properties	Formula	Source
Thermal conductivity $W/(m \bullet k)$	$k_a = \dfrac{770}{0.62(350 + T)} + 0.7$	Zoth [31]
Specific heat $J/(kg \bullet K)$	$C_{p,a} = 625(1 + T)^{0.075}$	Vosteen [32]
Density kg/m^3	$\rho_s = 2710$	Measured in this paper

$$k_{eff}(T) = \frac{hq(T)}{T_{upper} - T_{lower}} \tag{1}$$

where $k_{eff}(T)$ is the effective thermal conductivity of the steel fibre-reinforced AAC at the target temperature T, $q(T)$ is the average flux on the upper or lower boundary line obtained from the finite element analysis at the target temperature T, h is the height of the geometric model, $T_{upper} = T$+2.5, and $T_{lower} = T$-2.5 is the temperature applied at the upper and lower boundary lines.

The other is the transient analysis for determining the effective specific heat, in which all boundary conditions employed are the same as that used in the steady state analysis, and only difference is the initial condition which uses a relatively low temperature (T-2.5 °C) as the initial temperature in the domain. For each target temperature T, transient heat transfer analysis is conducted until it reaches to a steady state. The time histories of the temperature at the mid of the axisymmetric axis and the average heat fluxes at upper and lower boundary lines are used to calculate the effective specific heat of the steel fibre reinforced AAC, as shown below,

$$\rho_{eff} c_{eff} = \frac{\int_o^t (q_{upper} - q_{lower}) dt}{h \int_o^t \frac{dT_{mid}}{dt} dt} \tag{2}$$

where ρ_{eff} is the effective density of the steel fibre-reinforced AAC at the target temperature T, c_{eff} is the effective specific heat of the steel fibre-reinforced AAC at the target temperature T, q_{upper} and q_{lower} are the time histories of the average flux on the upper or lower boundary lines obtained from the finite element analysis at the target temperature T, respectively, and T_{mid} is the time history of the temperature at the mid of the axisymmetric axis obtained from the finite element analysis at the target temperature T. Note that the effective density of the steel fibre-reinforced AAC at the target temperature T can be assumed to be

$$\rho_{eff} = \rho_m V_m + \rho_a V_a + \rho_s V_s \tag{3}$$

where ρ_m, ρ_a, and ρ_s are the density of mortar, coarse aggregate, and steel fibre, and V_m, V_a, and V_s are the volume fraction of mortar, coarse aggregate, and steel fibre in the mix, respectively. Eqs. (1)–(3) are used to calculate the effective thermal properties of the steel fibre reinforced AAC.

The heat transfer finite element analysis in the present study is carried out using the commercial software COMSOL. The geometry of the three-phase finite element model is built using Voronoi method for coarse aggregate and Monte Carlo method for steel fibre; both are based on their volume fractions. The two-dimensional triangle plane elements of three nodes are used for mortar, coarse aggregate, and steel fibre. The continuity condition for temperature at the interface between different materials is assumed. In the present study, a mesh with varying element sizes was used where small element sizes were used surrounding the steel fibres and relatively large element sizes were used for the mortar matrix and aggregates. To ensure the results obtained have sufficient accuracy, a few trials with different meshing sizes [33] were carried out and the final mesh of 57000 elements was chosen when the result has almost no change while the element size was further reduced. Fig. 10 shows the schematic of the analysis model employed.
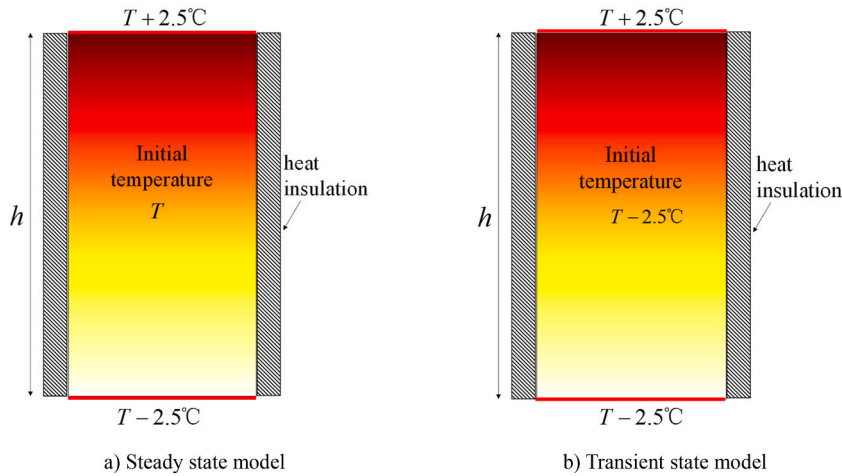
a) Steady state model b) Transient state model

Fig. 10. Schematic diagram for calculation of equivalent thermal parameters.

4.2. Experimental verification for the results of simulation

Fig. 11 plots the temperature distribution in the domain obtained from the finite element analysis of the steady state heat transfer. It can be observed from the figure that the temperature is not uniformly distributed along with the horizontal lines due to the influence of randomly distributed aggregates and steel fibres in the domain. Fig. 12 shows the comparison of the thermal proprieties between the three-phase model and experimental tests. The figure shows that the results obtained from the three-phase finite element analysis model match very well with the experimental results, which indicates that the effective thermal properties of the steel fibre-reinforced AAC can be predicted by using the multi-phase model if the thermal properties of individual components are known.

Based on the calibrated multi-phase finite element analysis model, a parametric study with varying volume fractions of steel fibre and coarse aggregate is also carried out. For steel fibre, its volume fraction is chosen from 0% to 3% with an interval of 0.5%. For coarse aggregate, its volume fraction is chosen from 0% to 30% with an interval of 5. The target temperature is chosen from 20 °C to 900 °C with an interval of 100 °C. In total, 490 (7 × 7 × 10) runs are executed. In each run the results related to the effective thermal conductivity, effective density, and effective specific heat are obtained, which are plotted in Figs. 13 and 14, respectively. It can be observed from Fig. 13 that, the increase in the steel fibre volume fraction results in an increase in the effective thermal conductivity; but the increasing rate is almost linear. Whereas the variation of the effective thermal conductivity with the coarse aggregate volume fraction is dependent on the temperature. For low temperature the effective thermal conductivity increases with the increased coarse aggregate volume fraction. But for high temperature the effective thermal conductivity decreases with the increased coarse aggregate volume fraction. It can be seen from Fig. 14 that, the volume fraction of the steel fibre has almost no effect on the effective specific heat; whereas the increase of the coarse aggregate volume fraction can slightly decrease the effective specific heat. The relationship between the effective specific heat and the coarse aggregate volume fraction is almost linear.

5. Conclusions

This paper has presented the experimental and numerical investigations on the thermal properties of AAM and AAC with and
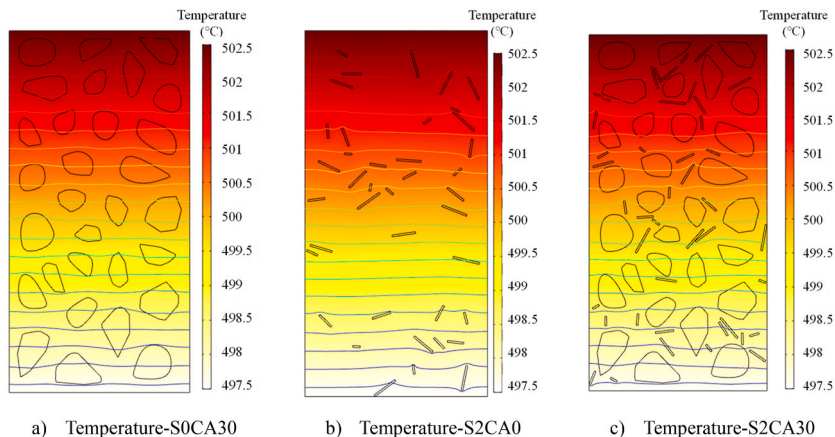

a) Temperature-S0CA30 b) Temperature-S2CA0 c) Temperature-S2CA30

Fig. 11. FEM model of the effective thermal parameters.

a) Thermal conductivity   b) Specific heat
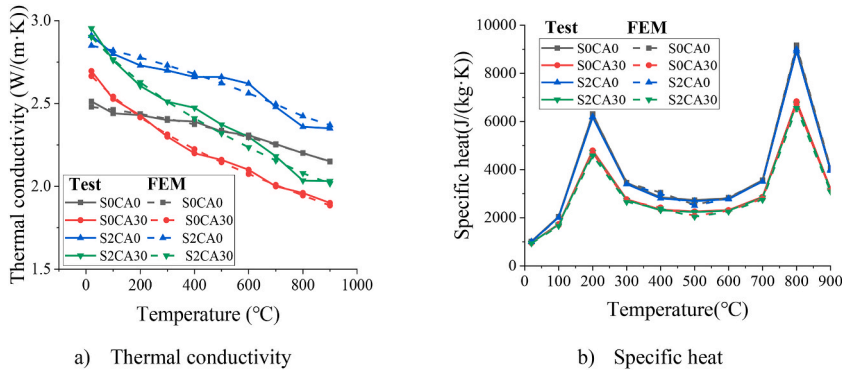
Fig. 12. FEM results compared with those of experiments.

a) Different steel fibre content   b) Different coarse aggregate content

Fig. 13. Simulated thermal conductivity.
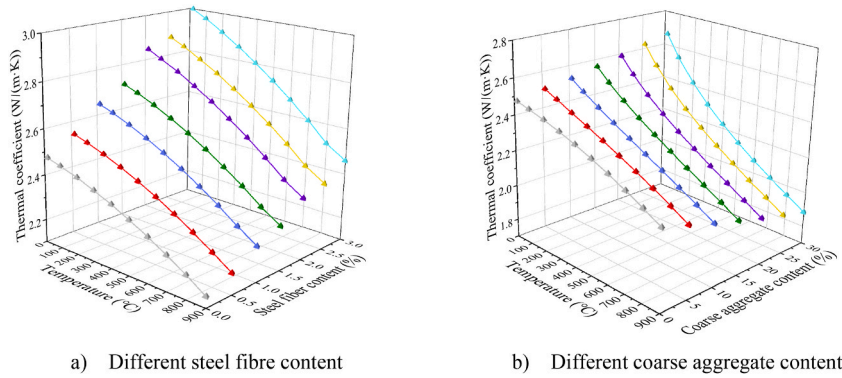

a) Different steel fibre content   b) Different coarse aggregate content
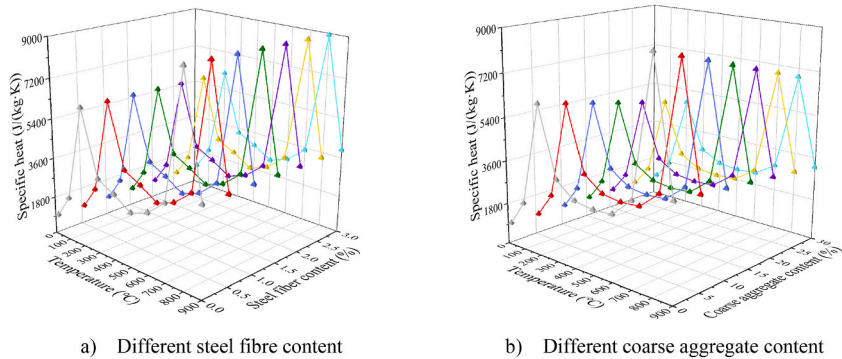
Fig. 14. Simulated specific heat.

without steel fibre when they are exposed to various elevated temperatures. The experimental work involves the tests to determine the temperature-dependent thermal conductivity, density, specific heat, and thermal expansion. The numerical work involves the development of multi-phase model which can be used to evaluate the effect of individual components on the effective thermal properties of the steel fibre reinforced AAC. From the results obtained the following conclusions can be drawn.

1) The steel fibre added in AAC can increase the thermal conductivity but has almost no effect on the specific heat and thermal expansion coefficient of the mixed AAC. The relationship between the effective thermal conductivity of the steel fibre reinforced AAC and the steel fibre volume fraction can be approximately treated as a linear function.

2) The influence of the coarse aggregate on the thermal properties of AAC is dependent on the temperature. For low temperature, the effective thermal conductivity increases with the increased coarse aggregate volume fraction; but for high temperature it decreases with the increased coarse aggregate volume fraction. The increase of the coarse aggregate volume fraction can slightly decrease the effective specific heat, but can largely increase the thermal expansion of the mixed AAC, particularly when the temperature is high.

3) The mass loss is quicker in the AAM than in the AAC. The mass loss in the AAM or AAC with steel fibre is slightly slower than that in the AAM or AAC without steel fibre. The quick mass loss was found in the two temperature ranges; one is between 100 °C and 300 °C; and the other is between 500 °C and 700 °C.

4) The thermal conductivity of AAC or AAM during heating process decreases with the increase of temperature. The decrease is much quicker in the AAC than in the AAM, and is slightly quicker in the steel fibre-reinforced AAC or AAM than in the non-reinforced AAC or AAM. The thermal conductivity of the AAC or AAM during cooling process does not change very much with the temperature.

5) The variation of the specific heat with temperature follows the up-down-flatten-up-down pattern. The first peak is around 200 °C and the second one is at about 800 °C. The two "going up" parts correspond to the slow temperature increase in the temperature-history curve of the sample, whereas the two "going down" parts correspond to the fast temperature increase in the temperature-history curve of the sample.

6) The linear thermal expansion of AAC is dependent on both the volume fraction of aggregate and temperature. For the AAC studied in the present study the linear thermal expansion increases with the increased temperature until the temperature reaches to 500 °C. After then it decreases with the further increased temperature. After the temperature exceeds 800 °C, it has some recovery.

7) The effective thermal properties of steel fibre reinforced AAC can be evaluated by using the multi-phase model of composites if the thermal properties of individual components used in the mixture are known. Voronoi method and Monte Carlo method can be used to generate the randomly, discretely distributed coarse aggregate and steel fibre in the multi-phase model of the steel fibre reinforced AAC based on their volume fractions.

Declaration of competing interest

The authors declare that they have no known competing financial interests or personal relationships that could have appeared to influence the work reported in this paper.

Data availability

No data was used for the research described in the article.

Acknowledgements

References

[1] M.S. Imbabi, C. Carrigan, S. McKenna, Trends and developments in green cement and concrete technology, Int. J. Sustain.Built. Environ. 1 (2) (2012) 194–216.

[2] P. Zhang, K. Wang, Q. Li, J. Wang, Y. Ling, Fabrication and engineering properties of concretes based on geopolymers/alkali-activated binders - a review, J. Clean. Prod. 258 (2020), 120896.

[3] F.A. Shilar, S.V. Ganachari, V.B. Patil, K.S. Nisar, Evaluation of structural performances of metakaolin based geopolymer concrete, J. Mater. Res. Technol. 20 (2022) 3208–3228.

[4] M.T. Ghafoor, Q.S. Khan, A.U. Qazi, M.N. Sheikh, M.N.S. Hadi, Influence of alkaline activators on the mechanical properties of fly ash based geopolymer concrete cured at ambient temperature, Construct. Build. Mater. 273 (2021) 121752.

[5] A. Bouaissi, L.Y. Li, M.M.A.B. Abdullah, Q. Bui, Mechanical properties and microstructure analysis of FA-GGBS-HMNS based geopolymer concrete, Construct. Build. Mater. 210 (2019) 198–209.

[6] World Business Council for Sustainable Development, Cement Technology Roadmap 2009: Carbon Emissions Reductions up to 2050, IEA technology roadmaps, WBCSD, 2009, 3940388475, 9783940388476).

[7] M.S. Eisa, M.E. Basiouny, E.A. Fahmy, Drying shrinkage and thermal expansion of metakaolin-based geopolymer concrete pavement reinforced with biaxial geogrid, Case Stud. Constr. Mater. 17 (2022) e1415.

[8] C. Oesterlee, H. Sadouki, E. Brühwiler, Structural Analysis of a Composite Bridge Girder Combining UHPFRC and Reinforced Concrete, University of Kassel, 2008.

[9] A. Kamen, Comportement au jeune âge et différé d'un bfup écrouissant sous les effets thermomécaniques, EPFL, Lausanne, 2007.

[10] T. Wang, M. Yu, W. Shan, L. Xu, S. Cheng, L.Y. Li, Post-fire compressive stress–strain behaviour of steel fibre reinforced recycled aggregate concrete, Compos. Struct. 309 (2023), 116735.

[11] H.R. Pakravan, M. Latifi, M. Jamshidi, Hybrid short fiber reinforcement system in concrete: a review, Construct. Build. Mater. 142 (2017) 280–294.

[12] P. Zhang, C. Wang, Z. Gao, F. Wang, A review on fracture properties of steel fiber reinforced concrete, J. Build. Eng. 67 (2023), 105975.

[13] F. Wu, L. Xu, Y. Chi, Y. Zeng, F. Deng, Q. Chen, Compressive and flexural properties of ultra-high performance fiber-reinforced cementitious composite: the effect of coarse aggregate, Compos. Struct. 236 (2020), 111810.

[14] K. Kim, S. Jeon, S. Kim, S. Yang, An experimental study on thermal conductivity of concrete, Cement Concr. Res. 33 (3) (2003) 363–371.

[15] V. Kodur, W. Khaliq, Effect of temperature on thermal properties of different types of high-strength concrete, J. Mater. Civ. Eng. 23 (6) (2011) 793–801.

[16] W. Khaliq, V. Kodur, Thermal and mechanical properties of fiber reinforced high performance self-consolidating concrete at elevated temperatures, Cement Concr. Res. 41 (11) (2011) 1112–1122.

[17] Y. Ju, H. Liu, J. Liu, K. Tian, S. Wei, S. Hao, Investigation on thermophysical properties of reactive powder concrete, Sci. China Technol. Sci. 54 (12) (2011) 3382–3403.

[18] T.Z. Harmathy, L.W. Allen, Thermal properties of selected masonry unit concretes, Int. Concr. Abstr. Portal(Am. Concr. Inst.) 70 (2) (1973) 132–142.

[19] L.T. Phan, Fire Performance of High-Strength Concrete: A Report of the State-Of-The-Art, National Institute of Standards and Technology, 1996, 199708.

[20] W.Z. Zheng, R. Wang, Y. Wang, Experimental study on thermal parameter of reactive powder concrete, J. Build. Struct. 35 (9) (2014) 107–114.

[21] W.H. Johnson, W.H. Parsons, Thermal expansion of concrete aggregate materials, J. Res. Natl. Bur. Stand. 32 (1944) 101–126.

[22] M. Ghannam, Proposed models for concrete thermal expansion with different aggregate types and saturation conditions, SN Appl. Sci. 1 (2019) 425.

[23] M.S. Siddiqui, D.W. Fowler, A systematic optimization technique for the coefficient of thermal expansion of Portland cement concrete, Construct. Build. Mater. 88 (2015) 204–211.
[24] J.A. Purkiss, L.Y. Li, Fire Safety Engineering, Design of Structures, third ed., CRC Press, Oxford, 2013.
[25] American Society of Civil Engineers, Structural Fire Protection, 1992. New York, USA.
[26] GB/T 5990-2021, Refractory Materials-Determination of Thermal Conductivity, Specific Heat Capacity and Thermal Diffusivity, Hot-Wire Method), Beijing, China, 2021.
[27] ASTM, Standard Test Method for Linear Thermal Expansion of Solid Materials by Thermomechanical Analysis, American National Standards Institute, 2019, E831–E142014.
[28] C. Kuenzel, L.M. Grover, L. Vandeperre, A.R. Boccaccini, C.R. Cheeseman, Production of nepheline/quartz ceramics from geopolymer mortars, J. Eur. Ceram. Soc. 33 (2) (2013) 251–258.
[29] P. Duxson, G.C. Lukey, J.S.J. van Deventer, Evolution of gel structure during thermal processing of na-geopolymer gels, Langmuir 22 (21) (2006) 8750–8757.
[30] T.T. Lie, Fire resistance of circular steel columns filled with bar in reinforced concrete, J. Struct. Eng. 120 (5) (1994) 1489–1509.
[31] R. Haenel, L. Stegena, L. Stegena, Handbook of Terrestrial Heat-Flow Density Determination, Solid Earth Sciences Library (SESL, vol. 4, Springer, 1988.
[32] H. Vosteen, R. Schellschmidt, Influence of temperature on thermal conductivity, thermal capacity and thermal diffusivity for different types of rock, Phys. Chem. Earth 28 (9/10/11) (2003) 499–509. Parts A/B/C.
[33] L.Y. Li, P. Bettess, J. Bull, T. Bond, I. Applegarth, Theoretical formulations for adaptive finite element computations, Commun. Numer. Methods Eng. 11 (10) (1995) 857–868.